

Creation of Topological Ultraslippy Surfaces for Droplet Motion Control

Xiaolong Yang, Kai Zhuang, Yao Lu,* and Xiaolei Wang*

Cite This: *ACS Nano* 2021, 15, 2589–2599

Read Online

ACCESS |

Metrics & More

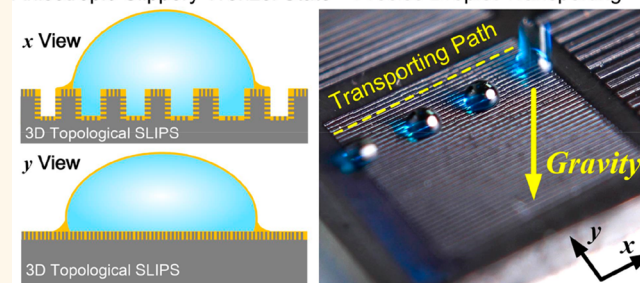
Article Recommendations

Supporting Information

ABSTRACT: Droplet motion control on slippery liquid-infused porous surfaces (SLIPS) that mimics the peristome surface of *Nepenthes alata* has promising applications in the fields of energy, lab-on-a-chip device, etc., yet is limited due to the difficulty in regulating its wettability. In this work, topologies with specific functions from natural creatures, for example, grooved structures of rice leaf and wedge-shaped structures of shore bird beak with droplet transporting capability were integrated with the SLIPS. Three-dimensional topological SLIPS was fabricated on metal substrates using laser milling followed by alkaline oxidation. Fabricated rice leaflike grooved nanotextured SLIPS can properly shape the droplet footprint to achieve a sliding resistance anisotropy of $109.8 \mu\text{N}$, which is 27 times larger than that of a natural rice leaf and can therefore be used to efficiently and precisely transport droplets; wedge-shaped nanotextured SLIPS can confine the droplet footprint and squeeze droplet to produce a Laplace pressure gradient for continuous self-driven droplet transport. The created surfaces can manipulate droplets of acid, alkali, and salt solutions. The proposed concept is believed to have potential applications for condensing heat transfer and droplet-based lab-on-a-chip devices.

KEYWORDS: slippery surface, droplet motion control, topology, superhydrophobic surface, nanotexture

Anisotropic-Slippy-Wenzel State Precise Droplet Transporting



Motion control of microliter droplets is a ubiquitous process in nature and is also crucial in the society systems¹ because of its wide applications in various fields, such as high-throughput cell screening,² high-accuracy molecular sensing,² microfluidic devices,³ enhanced heat transfer and water harvesting,⁴ biomedical testing,⁵ etc. Generally, lotus leaf-inspired superhydrophobic surfaces (water contact angle $>150^\circ$) with micro/nanotextures and low-surface-energy chemical components are regarded as representative materials for realizing droplet motion control by combining with (super) hydrophilic/hydrophobic patterns^{6,7} or by taking advantage of an external stimulus, for example, optical,^{8,9} electrical,^{10,11} thermal,¹² and magnetic signals.¹³ For example, Naoki *et al.* observed reversible topographical changes on a synthesized diarylethene microcrystalline surface by alternating UV and visible light irradiation;⁸ Dai *et al.* demonstrated a controllable high-speed droplet manipulation, for example, in-plane droplet moving and stopping/pinning in any direction without mass loss on superhydrophobic surface with electrostatic charging;¹⁰ Yang *et al.* prepared a smart, magnetically responsive superhydrophobic surface that comprised a dense array of magnetorheological elastomer micropillars by combining spray-coating and magnetic-field-directed self-assembly,

where the wettability and adhesion of droplets can be reversibly switched between the water-repellent and water-adhesive states by the on/off switching of an external magnetic field;¹³ Zahner *et al.* utilized photografting techniques to create superhydrophilic patterns on superhydrophobic porous polymer films, which allowed precise control of micro-sized droplets motion.¹⁴ However, droplet motion control on patterned superhydrophobic surfaces suffers from the defects of either mass loss on (super) hydrophilic patterns or limited droplet motion mode on hydrophobic patterns.¹⁵ Meanwhile, stimulus-responsive surfaces involve the external elements and therefore are not suitable for mild biomedical applications or engineering conditions where the stimulus cannot reach.¹⁶ In addition, most of these interfaces are difficult to manipulate liquids in rough situations because of the unstable air cushions in the surfaces.

Received: September 2, 2020

Accepted: November 24, 2020

Published: November 30, 2020



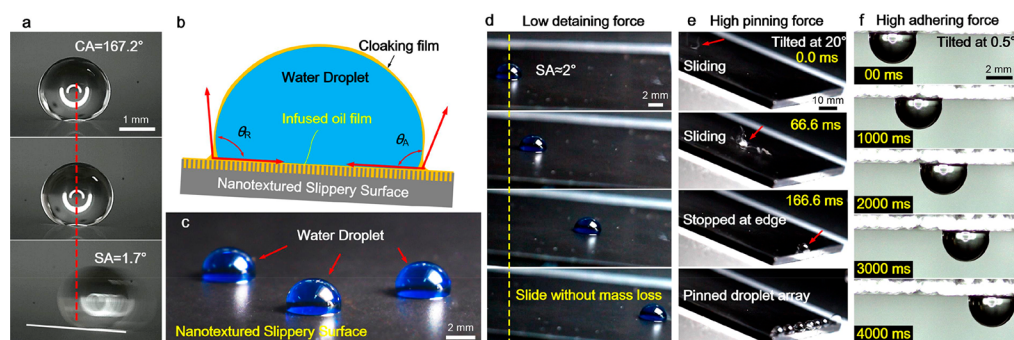


Figure 1. Spatial force anisotropy of droplets on the as-prepared nanotextured SLIPS: (a) sliding behavior of droplets on the superhydrophobic surface; (b) schematic and (c) digital photo of the nanotextured SLIPS with water droplets on it; time-lapse photos of a water droplet (d) sliding inside the SLIPS with low detaining force, (e) sliding and stopped at the edge of SLIPS due to high edge pinning force, and (f) sliding on an upside-down SLIPS because of the high perpendicular adhering force and low inside detaining force.

Instead, nature ubiquitously matches different solid and textures for the creation of exquisite functions: *Nepenthes* pitcher plant uses micro/nanotextures to lock an intermediary lubricant. Multilevel micro/nanotextures of the pitcher rim and well-matched surface energy enable the lubricant to completely fill the vacancy of the textures, creating a highly stable molecular-scale smooth film, where it is slippery enough to push the insects on the rim into the “stomach” by repelling the liquid on their legs. Inspired by the *Nepenthes* pitcher, Aizenberg *et al.* reported the concept of slippery liquid-infused porous surfaces (SLIPS) and proposed three principles that should be based for fabrication of stable SLIPS: (I) the substrate should have micro/nanotextures that the lubricant can completely wet and stably adhere; (II) surface energy must make the texture preferentially wetted by the lubricant rather than the liquid that is designed to be repelled; (III) the infused lubricant and repelled liquid must be immiscible.¹⁷ The fabricated SLIPS possesses characteristics such as ultralow contact angle hysteresis, self-healing, pressure stability, *etc.* According to the architecture of SLIPS system, droplet motion on SLIPS can be technically controlled by manipulating the physicochemical properties of the infused lubricant or the topology of the liquid-lubricant interface;^{5,17–22} the former element determines the wetting state and its contact angle, while the latter affects the energy barrier of droplet footprint movement. For instance, Aizenberg *et al.* reported that contact angle hysteresis of droplets on their proposed SLIPS decreased with the decreased surface tension of the tested liquid.¹⁷ Dai *et al.* proposed a Wenzel-state SLIPS with micropillar arrays. Droplets on the surface were in full contact with the top and sidewalls of the pillars, which created a discontinuous droplet footprint and therefore a large energy barrier for droplet movement.¹⁸ Inspired by the desert beetle’s bumpy topology in enhancing condensation and widening slope like cactus spines, Park prepared slippery asymmetric bumps with surrounding flat regions; on the fabricated SLIPS, condensed droplets moved effectively against the gravity because of the capillary force.²¹ Similarly, Huang *et al.* used a wedge-shaped slippery surface to promote the transport of a condensed droplet.²³ Ling fabricated bowl-like textures in a Y-shaped region on poly(dimethylsiloxane) (PDMS) substrates by using a microbead template; after it was infused with silicon oil, the surface was patterned ultraslippery and can be used as a microfluidic device to guide, transport, and mix droplets.²² After understanding that the physicochemical properties of the infused lubricant and the topology of the surface are the main

factors affecting the droplet motion on a slippery surface, we found some more sophisticated droplet manipulations can be achieved by introducing external stimuli such as temperature,^{24–26} electricity,^{27–31} magnetism,^{32–35} *etc.*, to *in situ* control those factors. For example, temperature-responsive adhesion control can be achieved by using temperature-dependent phase change materials like paraffin as the infuse liquid; the surface is hydrophobic with high adhesion when paraffin is solidified; as the temperature increased, the surface turned into ultraslippery state.²⁴ Nada reported that a droplet on SLIPS can be impelled to move rapidly by alternating the surface tension via a thermal gradient. The transport velocity was 5 times higher than that on conventional substrates due to an ultraweak pinning effect of SLIPS.²⁵ A thermal gradient for droplet driving can also be created via near-infrared (NIR) light irradiation on SLIPS with Fe₃O₄ nanoparticles.²⁶ Electricity is another efficient tool for realizing reversible and *in situ* control over droplet motion on SLIPS; droplet sliding, pinning, oscillation, jetting, and mixing were demonstrated by introducing a dielectric elastomer to control the micro-morphology of an oil-infused interface of a poroelastic SLIPS.²⁸ A magnetic field can also be utilized to control the geometry and, thereby, the dynamic behavior of the infused liquid or the above droplet when dropping Fe particles in it.³² Significant progress has been achieved on droplet motion control; however, the magnitude, directionality, and even uniformity of the control across the entire surface are limited; as a result, programming and performing more sophisticated and efficient droplet motion control is hindered.

Herein, we report three-dimensional (3D) topological SLIPS with anisotropic-slippery-Wenzel state inspired by the combination of sub-millimeter rice leaflike grooved structures and the nanotextured slippery configuration of *Nepenthes* pitcher. The sliding resistance anisotropy of the surface is $\sim 109.8 \mu\text{N}$ across the whole surface, which is ~ 27 times larger than that of the natural rice leaf³⁶ and can therefore be used to transport droplets efficiently and precisely with the aid of gravity. Meanwhile, self-driven droplet transport can also be achieved by confining the droplet footprint and squeezing the droplet to an egg shape to produce a Laplace pressure gradient using the integration of nanotextured SLIPS and the wedge-shaped structure of a shore bird beak. To meet the requirement of creating the designed 3D topological SLIPS surface, the fabrication process consisting of UV-laser-milling a sub-millimeter 3D structure and alkaline oxidizing nano-textures was used. This promising combinative surface as

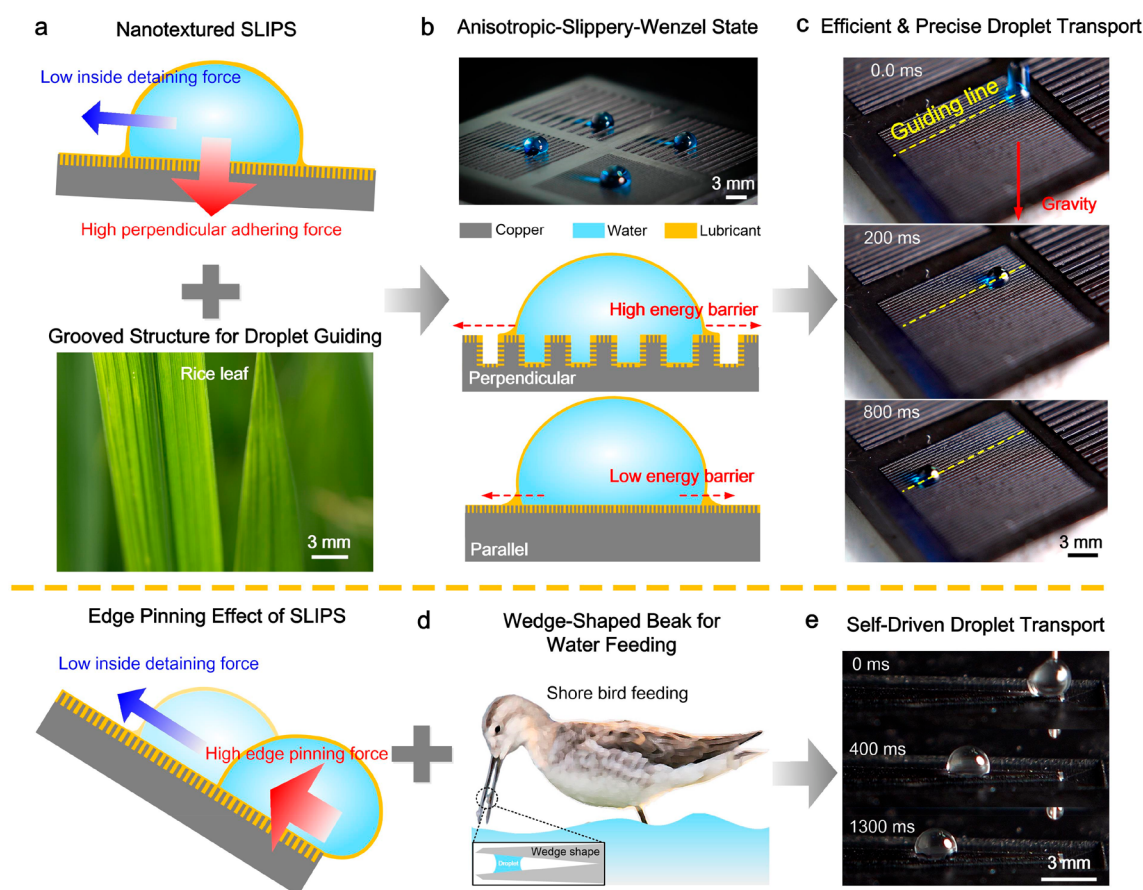


Figure 2. Strategy of creating 3D topological SLIPS for droplet motion control: (a) schematic of the force anisotropy of SLIPS and digital photo of a natural rice leaf; (b) photo of the grooved nanotextured SLIPS in anisotropic-slippy-Wenzel state and schematic of the wetting state parallel and perpendicular to the grooves; (c) time-lapse photos of efficient and precise droplet transport on the grooved nanotextured SLIPS; (d) schematic of the force anisotropy of the SLIPS and a shore bird feeding water using beak with wedge-shaped opening; (e) time-lapse photos of self-driven droplet transport on the wedge-shaped nanotextured SLIPS.

well as the proposed fabrication techniques in this work have great potential for applications in the precise control of microdroplets, biomedical testing, microfluidic devices, and enhanced condensing.^{37,38} These concepts can be extended to more sophisticated topologies for autonomous droplet motion control by introducing specific materials and external stimuli for different purposes.

RESULTS AND DISCUSSION

Design of 3D Topological SLIPS for Droplet Motion Control. The copper surface subjected to alkaline oxidation was nanotextured in order to achieve a stable Cassie-state superhydrophobicity after a reduction in surface energy via a chemical modification. A 5 μL water droplet dispensed on the as-prepared surface had a contact angle of 167.2° and a sliding angle of 1.7° , exhibiting excellent static and dynamic superhydrophobicity (Figure 1a). After an infusion with silicon oil, the surface turned into SLIPS with nanotextures imbuing a uniform thin oil lubricant. Water droplets dispensed on as-prepared SLIPS were cloaked by the lubricant beneath, had small contact angles ($111.5^\circ \pm 2.4^\circ$) with large footprints (Figure 1b,c), and showed interesting anisotropic dynamic behavior. For example, a droplet slid easily inside the surface at a tilting angle of only 2° due to an ultralow detaining force (Figure 1d and Movie S1), but it was then stopped at the edge due to the high pinning force (Figure 1e and Movie S2).

Despite the ultralow detaining force inside the surface, the droplet adhering force perpendicular to the surface is extremely high due to the high contact energy between the droplet and the SLIPS, which can hang the droplet on an upside-down SLIPS and allow it to slide at a tilting angle of only 0.5° (Figure 1f and Movie S3). It is thus clear that the detaining force inside SLIPS, the pinning force at the edge of the surface, and the adhering force perpendicular to the surface are quite different, showing obvious spatial anisotropy.

By taking advantage of the spatial force anisotropy of a nanotextured SLIPS and combining specific 3D structures of natural creatures with droplet-guiding capability, 3D topological SLIPS with enhanced and diverse anisotropic dynamic behavior can thereby be created for sophisticated droplet motion control (Figure 2). For instance, sub-millimeter grooved veins on rice leaf can guide a droplet to move along the vein to the root of the leaf for essential water supplies. Inspired by the sub-millimeter grooved structures of rice leaf and the anisotropy between the inside detaining force and the perpendicular adhering force as shown Figure 2a, a grooved nanotextured SLIPS in an anisotropic-slippy-Wenzel state (Figure 2b) can be created by machining sub-millimeter grooved structures with laser milling, creating nanotextures on the groove surface via alkaline oxidation, reducing surface energy, and subsequently subjecting to an oil infusion. The sliding resistance anisotropy between the parallel and

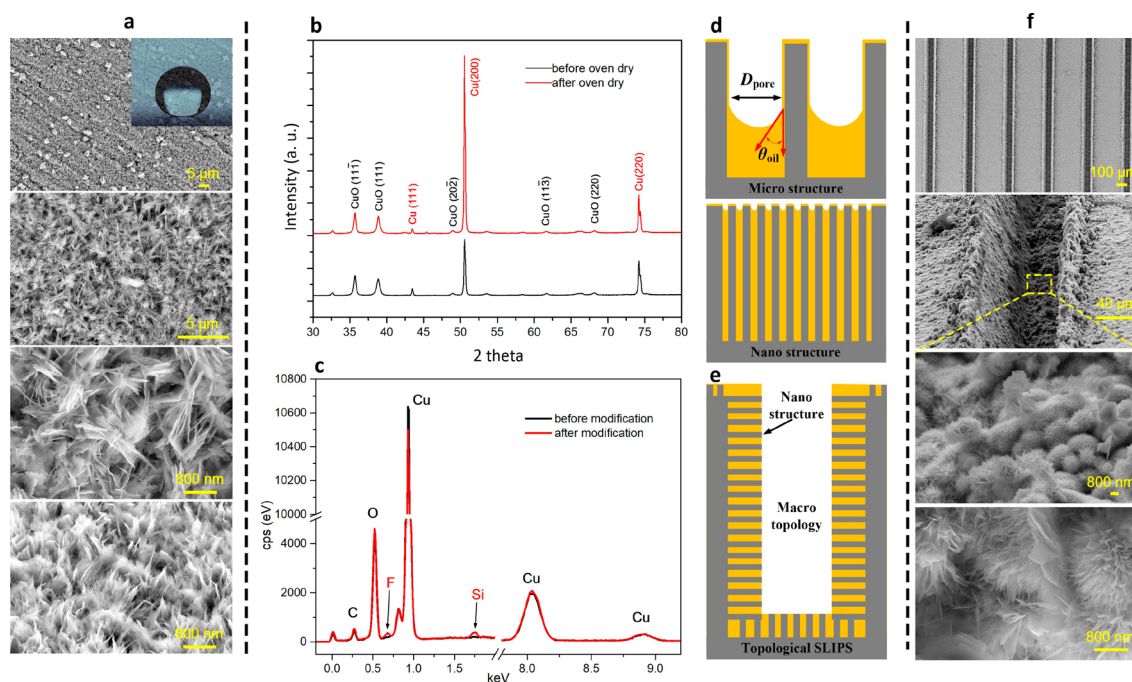


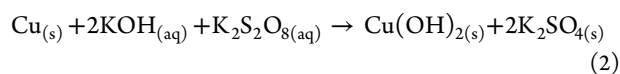
Figure 3. Morphology and chemical component of the fabricated surface: (a) SEM images of nanograss on a plain copper surface that was only treated by alkaline oxidation; (b) XRD spectra of the nanotextures before and after the drying process; (c) EDS spectra of the nanotextures before and after hydrophobization; (d) schematic of oil infusion in micro- and nanoscale textures; (e) schematic of oil infusion in 3D topological textures; (f) SEM images of the surface that was treated by laser milling and subsequent alkaline oxidation; a dense nanograss produced by alkaline oxidation was detected on the laser-milled groove surface.

perpendicular grooves of this 3D topological SLIPS is $\sim 109.8 \mu\text{N}$ across the whole surface, which is ~ 27 times larger than that of the natural rice leaf. The sliding resistance was obtained according to the force equilibrium

$$F = mg \sin \alpha \quad (1)$$

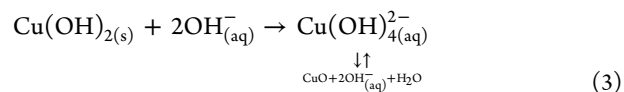
where m is the droplet mass, g is the acceleration of gravity, and α is the measured sliding angle. The data of the sliding resistance anisotropy were obtained by calculating the difference between the perpendicular and parallel sliding resistance. Because of the significant sliding resistance anisotropy, the surface can be used to transport droplets efficiently and precisely along a designed track, even off the gravity direction by 63° (Figure 2c and Movie S4). In addition, by integrating the anisotropy between the inside detaining force and the edge pinning force (Figure 2d), with a wedge shape analogous to the beak that is used by shore bird to implement Laplace-pressure-driven water feeding, wedge-shaped nanotextured SLIPS can be created to confine the droplet footprint and squeeze the droplet into an egglike shape to generate a Laplace gradient for continuous droplet transport (Figure 2e and Movie S5).

Construction of the SLIPS. The SLIPS was constructed by creating nanotextures on the copper substrates via alkaline oxidation, reducing surface energy for superhydrophobicity, and subsequently subjecting to oil infusion to obtain a lubricating layer. Alkaline oxidation in aqueous solution creates $\text{Cu}(\text{OH})_2$ according to³⁹



However, $\text{Cu}(\text{OH})_2$ is metastable; as a result, $\text{Cu}(\text{OH})_2$ was subsequently transformed into CuO through a reconstructive

process involving a dissolution reaction and the following precipitation.⁴⁰



This two-step reaction makes $\text{Cu}(\text{OH})_2$ rapidly transform into CuO in alkaline solution even at 70°C . Thanks to the reconstructive process, nanograss textures were formed on the copper substrates (Figure 3a). XRD patterns of the oxidized surface were demonstrated in Figure 3b. Five main diffraction peaks at 35.5° , 38.7° , 48.7° , 61.7° , and 68.4° , which correspond to the $(11\bar{1})$, (111) , $(20\bar{2})$, $(11\bar{3})$, and (220) crystal planes of CuO , respectively, were detected on the surface both before and after the drying process, while peaks of $\text{Cu}(\text{OH})_2$ were not found,⁴¹ which again verified that the dehydration process was already completed in the alkaline oxidation process in the solution. After chemical modification in an fluoroalkylsilane (FAS) ethanol solution, elements of C, O, Si, and F were detected via energy-dispersive spectroscopy (EDS) (Figure 3c), which demonstrated that the low surface energy groups of Si–O–Si and C–F were successfully assembled on the surface.⁴² These nanograss textures were rough enough to achieve stable Cassie-state superhydrophobicity after lowering the surface energy via chemical modification. A $5 \mu\text{L}$ water droplet dispensed on the as-prepared surface had a contact angle of 167.2° and a sliding angle of 1.7° , exhibiting excellent static and dynamic superhydrophobicity. However, the surface can be completely wetted by silicon oils, forming a uniform lubricating layer because of their ultralow surface tension ($\gamma_o = 20 \text{ mN}\cdot\text{m}^{-1}$) compared with that of water ($\gamma_{wa} = 72 \text{ mN}\cdot\text{m}^{-1}$).²⁵ The silicon oil has absolute priority to wet the superhydrophobic surface

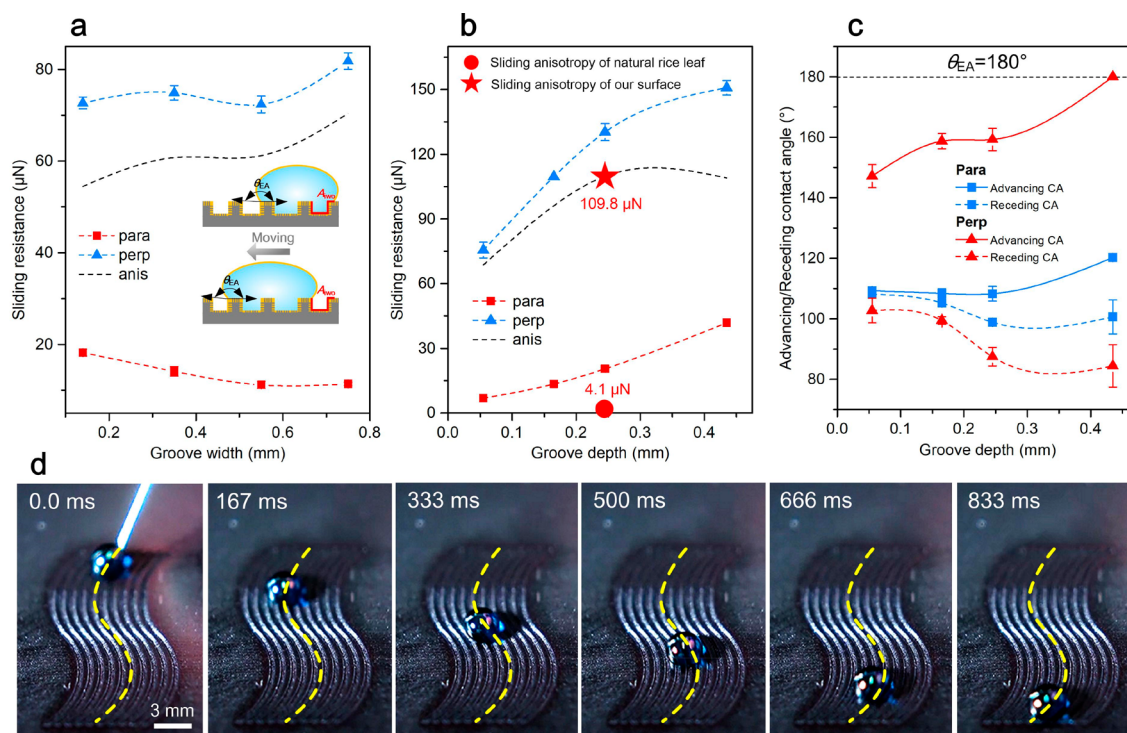


Figure 4. Droplet motion control on a grooved nanotextured SLIPS that was fabricated by the combination of sub-millimeter grooved structures of rice leaf and nanograss on the groove surfaces: sliding resistance parallel and perpendicular to the grooves as a function of (a) groove width and (b) groove depth, the groove depth in (a) is 0.05 mm, while the groove width in (b) is maintained at 0.37 mm; the data of sliding resistance anisotropy were obtained by calculating the difference between perpendicular and parallel sliding resistance; (c) advancing and receding contact angles as a function of groove depth; (d) time-lapse photos of transporting water droplets with the aid of gravity on winding grooved nanotextured SLIPS; the groove width is 0.35 mm, and the surface was tilted at $\sim 20^\circ$.

and is immiscible with water; as a result, the oil adhered in the nanotextures and functioned as the lubricant. Philseok *et al.* proposed that, unlike a lotus leaf effect, which generally prefers hierarchical micronano textures for the improved stability of a Cassie state, nanotextures provide the most shear-tolerant oil-infused slippery behavior.⁴³ Herein, we further identified Philseok's conclusion by using a capillary force equation and experimental observation. As shown in Figure 3d, the lubricant infused in porous textures has the tendency to climb to the top of the surface due to the capillary force F_{cp} , which can be described using the following equation.⁴⁴

$$F_{cp} = \frac{4\gamma_o \cos \theta_{oil}}{D_{pore}} \quad (4)$$

Once the surface tension of lubricant γ_o and the contact angle of the materials θ_{oil} are fixed, the capillary force for the lubricant F_{cp} is inversely proportional to the equivalent diameter D_{pore} of the porous texture. The lubricant in a nanotextured porous has an adequate driving force to climb to the top of the surface, imbuing the textures to generate a uniform lubricant layer except some meniscus on the top surface (Figure 1c and Figure S2). On the contrary, for microtextured pores, a lubricant has limited F_{cp} to occupy all the rough morphology of the surface, which generally produces a lubricant defect (Figure 3d). It is thus clear that nanotextures are crucial for the creation of SLIPS, while microtextures are not necessary, as they have the possibility to produce lubricant defects.

Thanks to the uniform lubricating layer generated on the nanotextures, 3D topological SLIPS can therefore be

constructed by combining sub-millimeter 3D structures and the on-top nanotextures for lubricating (Figure 3e). The grooved nanotextured SLIPS was successfully fabricated using a UV laser to mill sub-millimeter grooved structures (Figure S3) and subsequently apply alkaline oxidation to produce nanograss textures on the groove surface. SEM images in Figure 3f showed that dense nanograss textures covered the grooves without changing its sub-millimeter grooved structure, forming a multilevel 3D topological configuration. After being subjected to chemical modification to reduce the surface energy and infuse silicon oil, SLIPS with 3D topology was therefore obtained as sketched in Figure 3e.

Static and Dynamic Wetting Behavior on the 3D Topological SLIPS. Unlike the liquid–solid interface on a superhydrophobic surface, a water droplet on a SLIPS contacts oil lubricant directly and oil may spread along the liquid–air interface, cloaking the water droplet (Figure 1b). The condition for cloaking is given by the spreading coefficient

$$S_{ck} = \gamma_{wa} - \gamma_{wo} - \gamma_{oa} \quad (5)$$

where γ_{wa} , γ_{wo} , and γ_{oa} represent the surface tension of the water–air, water–oil, and oil–air interfaces, respectively. Positive S_{ck} indicates cloaking, while a negative value implies otherwise.⁴⁵ Silicon oil was used as the lubricant in this work; the spreading coefficient was thereby calculated to $10 \text{ mN}\cdot\text{m}^{-1}$ by using the 72, 42, and $20 \text{ mN}\cdot\text{m}^{-1}$ values for γ_{wa} , γ_{wo} , and γ_{oa} , respectively, manifesting that the lubricant cloaked the water droplet. This can also be identified by the phenomenon of cloaking lubricant flowing on the droplet interface (Movie S6). The cloaked water droplet on the SLIPS appeared like a spherical cap with a large footprint, showing a different shape

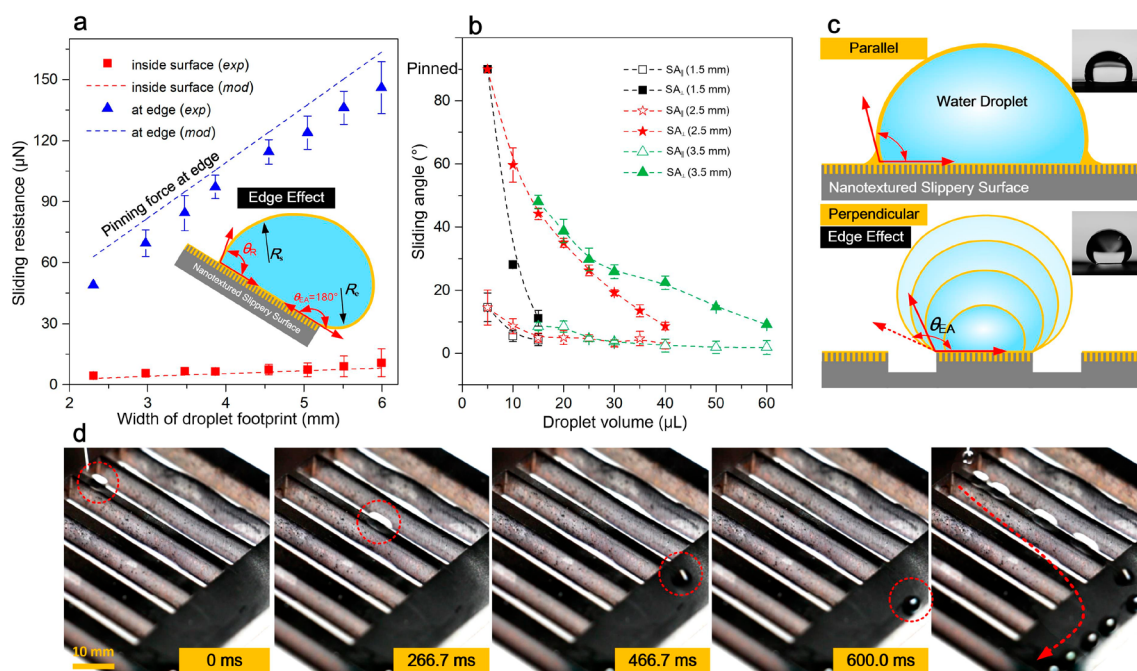


Figure 5. Edge effect of nanotextured SLIPS: (a) experimentally measured and model-predicted sliding resistance of droplets inside and at the edge of SLIPS; (b) parallel and perpendicular sliding angle of droplets on strip-ridge-shaped nanotextured SLIPS with sharp edge; (c) schematic of footprint evolution inside and at the edge of SLIPS; (d) time-lapse photos of guiding water droplet movement using a strip-ridge-shaped nanotextured SLIPS with a ridge width of 1.5 mm.

from the spherical-like beads on the superhydrophobic surfaces (Figure 1c). The apparent contact angle θ on SLIPS is given by the modified Young's equation.

$$\cos \theta = \frac{\gamma_o - \gamma_{ow}}{\gamma_o + \gamma_{ow}} \quad (6)$$

By using the equation, θ can be deduced to $\sim 110.8^\circ$, which is close to the experimentally measured value of $111.5^\circ \pm 2.4^\circ$. On the one hand, despite the relatively small contact angle and large footprint, the water droplet easily slid inside the surface with an ultralow sliding angle ($\sim 2^\circ$) but hardly changed its shape during the motion due to the uniform lubricating layer and liquid–liquid interface with an ultralow detaining force. On the other hand, the contact angle θ and the area of footprint A_{wo} determine the contact energy, which has a positive relationship with the perpendicular adhering force F_d of the droplet, given by the Young–Dupre equation.^{46,47}

$$F_d \propto E_d = \gamma_{wo}(1 + \cos \theta)A_{wo} \quad (7)$$

For SLIPS, small θ and large A_{wo} generate increased F_d ; therefore, a droplet impacting on both horizontal and tilted SLIPS would be dragged by the F_d during the rebounding process, resulting in a low rebounding height and a splitting satellite droplet (Figure S4), which was different from the droplet bouncing behavior on superhydrophobic surfaces.⁴⁸

Knowing the rules of ultralow inside detaining force and high perpendicular adhering force on SLIPS, a 3D topological SLIPS in an anisotropic-slippy-Wenzel state (Figure 2b) can be created for more sophisticated droplet manipulations by the combination of sub-millimeter rice leaflike grooved structures and nanogras on the grooves (Figure 2a). For a solid–liquid interface, textures with high roughness enlarge the contact energy, making liquid fully contact with the textured solid substrates (Wenzel state). Similarly, for a liquid–liquid

interface of SLIPS, the water droplet dispensed on the grooved nanotextured SLIPS would be cloaked, then sucked and adhered firmly into the 3D topology, establishing anisotropic-slippy-Wenzel state (see the Supporting Information, Movie S7). Profiles of the grooves can be found in Figure S5. A droplet sliding parallel to the grooves had a low energy barrier, the same as sliding on a homogeneous SLIPS due to the continuous footprint interface; however, droplets need to overcome a high energy barrier because of the large adhering force when moving perpendicular to the grooves. Sliding resistance parallel and perpendicular to the grooves measured in the experiments further confirmed the significant sliding anisotropy (Figure 4a). The experimental measurements showed that the sliding anisotropy increased slightly with the increased groove width, because, when moving across a groove with a large width, a droplet needs to overcome a higher contact energy produced by the large inner surface area A_{wo} (inset of Figure 4a) of the grooves according to eq 7. Similarly, the sliding anisotropy also showed a significant increase with the increased groove depth (Figure 4b, also see Supporting Information, Movie S8). A groove with a large depth not only has a large contact energy (energy barrier) for perpendicular moving due to the large contact area A_{wo} but also produces a high downward Laplace pressure, which further increases the perpendicular sliding resistance. Figure 4c displayed that the contact angle hysteresis perpendicular to the grooves increased sharply with the groove depth. The largest sliding resistance anisotropy on the grooved nanotextured SLIPS inspired by the combination rice leaf and *Nepenthes* pitcher is $\sim 109.8 \mu\text{N}$, which is 27 times larger than that of a natural rice leaf ($4.1 \mu\text{N}$). This combination endowed the artificial surface with anisotropic-slippy-Wenzel-state wettability. In this case, droplets exhibit significant sliding anisotropy across the whole surface, which can be utilized to achieve droplet motion control in a more efficient and stable way compared with

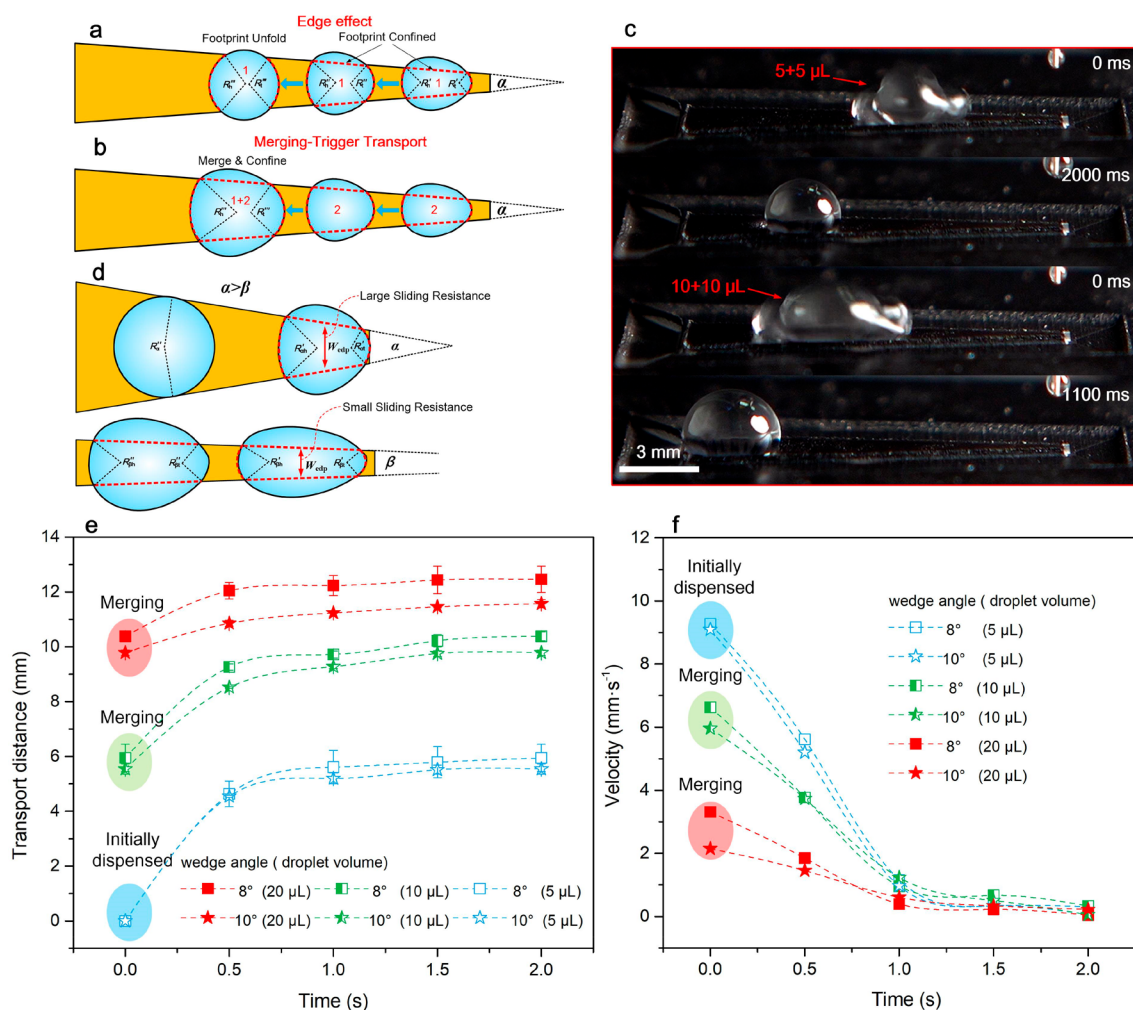


Figure 6. Self-driven droplet transport on wedge-shaped nanotextured SLIPS: (a) schematic of self-driven droplet transport on SLIPS; (b) schematic of merging-trigger self-driven droplet transport on SLIPS; (c) time-lapse photos of transporting a 20 μL droplet on SLIPS with a wedge angle of 8° using the merging-triggered transport process; (d) schematic showing the influence of wedge angle on the driving force and sliding resistance for droplet transport; (e) transport distance and (f) velocity as a function of droplet volumes on wedge-shaped nanotextured SLIPS with different wedge angles. Note that the volumes of 10 and 20 μL were the data for the merged droplet in the merging-triggered self-driven transport process instead of the initially dispensed droplet.

previous works, which generally use a hydrophilic line to guide the droplet movement.^{49,50} As shown in time-lapse photos in Figure 4d, a droplet was transported exactly along winding grooves (Movie S9). More dynamic behavior of droplets on the grooved nanotextured SLIPS with anisotropic-slippy-Wenzel state can be found in Movie S10. In practical microfluidic applications, the manipulated liquid could be acid, alkali, and salt solution; therefore, dynamic behavior including perpendicular and parallel sliding resistance, as well as the sliding anisotropy of droplets of 5 wt % salt (NaCl), acid (CH_3COOH), and alkali (NaHCO_3) solutions as a function of the groove width and groove depth on the grooved nanotextured SLIPS were measured (Figure S6a–d). Results showed no significant difference from the data of deionized water. Droplets of the acid, alkali, and salt solutions can be efficiently transported by using the grooved nanotextured SLIPS (Figure S6e,f and Movie S11). For demonstrating the feasibility of diverse droplet manipulations, droplet storage and mixing were also implemented by using the grooved nanotextured SLIPS (Figure S7 and Movie S12).

In addition to the high perpendicular adhering force on SLIPS, which can be used to create a surface with anisotropic-slippy-Wenzel-state for precise droplet transport, another interesting phenomenon was that water droplets easily slid inside SLIPS with droplet shape hardly changing but would be pinned at the edge of the surface, which was rather different from the situation of a superhydrophobic surface (Figure 1e). This is ascribed to the SLIPS having a small static contact angle, and the interface of the droplet footprint at the surface would be confined until the advancing contact angle θ_{EA} increased from 112.5° with small curvature C_s to 180° of water in air with large curvature C_1 before sliding off the surface (edge effect). The increment of inner Laplace pressure ΔP , which is proportional to curvature, can thereby be calculated using the following formula.⁴⁴

$$\Delta P \approx 2\gamma_{\text{wo}}(C_1 - C_s) = 2\gamma_{\text{wo}}\left(\frac{1}{R_e} - \frac{1}{R_s}\right) \quad (8)$$

Here, R_e and R_s represent the radii of a water droplet when sliding off the edge and inside the surface of SLIPS, respectively. The gravity component of a water droplet at the

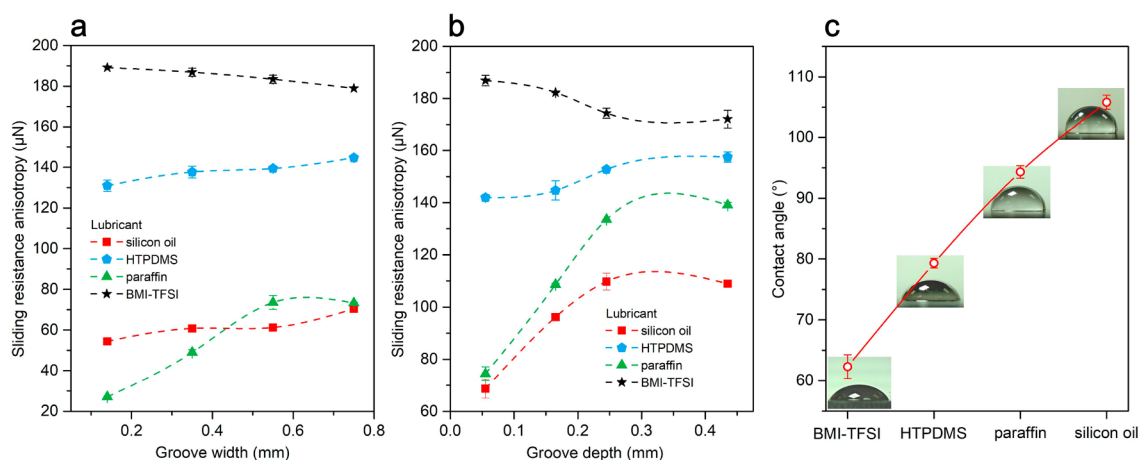


Figure 7. Static and dynamic wetting behavior on SLIPS that were infused with different lubricants: sliding resistance anisotropy as a function of (a) groove width and (b) groove depth; (c) water contact angle on the SLIPS.

edge is supposed to deform the droplet until ΔP reaches the threshold; as a result, the resistance for droplets sliding off the edge is significantly larger than that sliding inside the surface as depicted in Figure 5a. The sliding resistance on in-air and in-water superwetting surfaces can be well-described by a classical dragging resistance model, which is known as the Fumidge equation^{49–52}

$$F_{re} = \gamma \cdot W_{dp} (\cos \theta_R - \cos \theta_A) \quad (9)$$

where γ is the surface tension of the interface between the droplet and surrounding medium, W_{dp} is the interfacial width of droplet perpendicular to the sliding direction, while θ_R and θ_A represent receding and advancing contact angles, respectively. For cloaking SLIPS, a water–oil interfacial surface tension γ_{wo} was adopted as γ in the equation. The sliding resistance for inside and at the edge of SLIPS can then be predicted by using experimentally measured W_{dp} , θ_R , and θ_A as depicted in Figure 5a. Note that a key difference between the inside and at the edge of SLIPS is that θ_A is 112.5° inside the surface, while it is 180° at the edge. The θ_R value of 110.5° is constant for these two situations. As can be seen, the model that predicted a sliding resistance inside and at the edge of SLIPS exhibited an obvious anisotropy, showing a good agreement with the experimental measurements (Figure 5a). This edge-effect-induced anisotropic sliding was further verified by using a strip-ridge-shaped nanotextured SLIPS with a sharp edge. Sliding angle anisotropy parallel and perpendicular to the ridge was detected and was found to decrease with increased droplet volumes and decreased ridge width (Figure 5b). That is because the droplet on the SLIPS has a small contact angle hysteresis parallel to the ridge; meanwhile, the footprint of a droplet would be confined until θ_{EA} increased from the initial value to 180° before perpendicular sliding off the edge of the ridge (edge effect), which was the same as the situation of sliding off the edge of SLIPS. Both decreased ridge width and increased droplet volume would raise the initial value and accelerate the perpendicular sliding off process (Figure 5c). This sliding anisotropy caused by the footprint confinement of the edge effect can also be utilized to transport a water droplet efficiently without mass loss as demonstrated in the time-lapse photos in Figure 5d (Movie S13).

By taking advantage of the above-discussed edge effect, droplet transport without the need of gravity can be achieved

with a wedge-shaped nanotextured SLIPS. In the literature, self-driven droplet transport on a wedge-shaped SLIPS has been reported by Huang *et al.*,²³ but the underlying interfacial mechanism was not discussed. Herein, the edge effect was applied to explain this self-driven droplet transport process. As shown in Figure 6a, a droplet dispensed on the narrowing end of a wedge-shaped nanotextured SLIPS was squeezed along the wedge to the widening direction, resulting in an egglike shape with varied radius from the tail to the head, as the footprint was confined by the edge of SLIPS. The difference between the tail radius R_t and the head radius R_h of the droplet generates inner Laplace pressure gradient ΔP for the impelling force F_i , which can be qualitatively described by the following equation.

$$F_i \approx \Delta P \approx 2\gamma_{wo} \left(\frac{1}{R_t} - \frac{1}{R_h} \right) \quad (10)$$

In addition, the droplet should overcome the sliding resistance F_{re} , which is proportional to the equivalent interfacial width W_{edp} perpendicular to the sliding direction according to eq 9. As displayed in Movie S5, F_i can impel the droplet to move along the wedge to the widening direction. But as the movement proceeded, the difference between R_t and R_h , as well as the ΔP and the induced F_i , decreased gradually, until the squeezed droplet was unfolded to a level at which the impelling force was equal to the sliding resistance F_{re} (Figure 6a), and the droplet finally stopped. This forward movement can restart when the droplet grows bigger, and its footprint can then be confined again after merging with another dispensed droplet (labeled as Droplet 2 in Figure 6b). In this way, a droplet can be continuously transported by following the steps of merging-confined-transported as long as we keep dispensing droplets at the narrowing end of the wedge. For example, a $20 \mu\text{L}$ droplet was transported to the end of the wedge by using this merging-triggered transport for illustration (Figure 6c). For SLIPS with a smaller wedge angle, the droplet needed to be transported to a farther place to unfold its footprint, and the sliding resistance F_{re} during the transport was smaller than that with a large wedge angle because of the smaller equivalent interfacial width W_{edp} (Figure 6d); as a result, both the transported distance and velocity increased with the decreased wedge angle (Figure 6e,f).

The concept proposed in this work was demonstrated and discussed by using SLIPS that were infused by silicon oil,

which was a very common lubricant for fabricating SLIPS. However, the SLIPS would be invalid when the silicon oil volatilized under extreme circumstances, such as in vacuum. In addition, the water droplet was cloaked on the silicon oil-infused SLIPS; as a result, some applications, for example, cell screening and high-accuracy molecular sensing, cannot be achieved. However, the uncloaked situation was possible when a proper lubricant with a negative spreading coefficient was chosen. For instance, the ionic liquid (1-butyl-3-methylimidazolium bis (trifluoromethylsulfonyl) imide (BMI-TFSI) was used for the infusion to illustrate the feasibility. In this situation, lubricant loss through evaporation was not a concerning issue due to the extremely low vapor pressure ($\sim 1.33 \times 10^{-10}$ Pa)⁵³ of the ionic liquid, and the manipulated droplets would not be cloaked for meeting the requirement of direct sensing and screening, as the ionic liquid-infused SLIPS had a negative spreading coefficient S_{ck} ($-5 \text{ mN}\cdot\text{m}^{-1}$).^{45,54} To validate this assumption, grooved nanotextured SLIPS were fabricated by machining sub-millimeter grooved structures with micro/nano porous via laser milling, reducing the surface energy and subsequently infusing the ionic liquid (BMI-TFSI). The sliding resistance anisotropy of the ionic liquid-infused SLIPS was measured and compared with those infused by silicon oil, hydroxy-terminated poly(dimethylsiloxane) (HTPDMS), and liquid paraffin. The results showed that the sliding resistance anisotropy generally increased with the decreased water contact angle θ of the plain SLIPS (Figure 7a–c). This is ascribed to the small θ generating a large contact energy (energy barrier) for a droplet moving across the grooves. Therefore, the ionic liquid-infused SLIPS with a small θ had a large perpendicular sliding resistance and a significant sliding resistance anisotropy (Figure S8 and Movie S14). The feasibility of fabricating diverse 3D topological SLIPS that were infused with different liquids provided alternates for more applications in both lab-on-a-chip and heat-transfer devices.

CONCLUSION

A configuration of 3D topological SLIPS was proposed to shape the droplet footprint and therefore control the droplet sliding resistance or inner Laplace pressure for droplet manipulations. A fabrication process that consists of laser-milling 3D structures and alkaline oxidation for creating nanogross was proposed, and this technique can be applied to fabricate large-area 3D topological SLIPS on both flat and curved metal substrates. Similar with a superhydrophobic Wenzel state, a droplet footprint made full contact with the 3D structure due to the high adhering force between the water droplet and the lubricant, resulting in an anisotropic-slippery-Wenzel state. The sliding anisotropy in this wettability state is 27 times larger than that of a natural rice leaf and is constant across the whole surface, which can be utilized to realize efficient and stable droplet transport. Moreover, applying more topologies to nanotextured SLIPS for diverse droplet manipulation is feasible, for example, inspired by shore bird beak, which feeds water using a Laplace pressure gradient induced by the wedge-shaped structure. A wedge-shaped nanotextured SLIPS was created to confine the droplet footprint and squeeze the droplet to produce a Laplace pressure gradient for continuous self-driven droplet transport.

The design strategy of the 3D topological SLIPS, fabrication process, and rules of droplet motion control on the surface can be extended to create functional surfaces for applications from

lab-on-a-chip devices to energy fields, for example, dropwise-enhanced heat-transfer components.

METHODS

Materials. Copper sheets ($40 \times 40 \times 3$ mm) were purchased from Suzhou Metal Material Manufacturer. Potassium persulfate ($\text{K}_2\text{S}_2\text{O}_8$) and potassium hydroxide (KOH) were purchased from Nanjing Reagent. Fluoroalkylsilane [FAS, $\text{C}_8\text{F}_{13}\text{H}_4\text{Si}(\text{OCH}_2\text{CH}_3)_3$] was purchased from Macklin Co. Ltd., and silicon oil (viscosity ~ 20 cst at 25°C) was obtained from Dow Corning Co. Ltd. HTPDMS (viscosity ~ 40 cst at 25°C), liquid paraffin (viscosity ~ 43 cst at 40°C), and ionic liquid (BMI-TFSI, viscosity ~ 51 at 25°C) were obtained from Sigma-Aldrich. All chemicals are analytically pure and were used as received.

Fabrication of Homogeneous Nanotextured SLIPS. The copper sheet was polished and cleaned in DI water before being oxidized in the mixed aqueous solution of $2.5 \text{ mol}\cdot\text{L}^{-1}$ KOH and $0.065 \text{ mol}\cdot\text{L}^{-1}$ $\text{K}_2\text{S}_2\text{O}_8$ at 70°C for 45 min. The oxidized sample was subsequently cleaned in DI water and subjected to a drying process at 200°C for an hour. After it was cooled, the sample was immersed in a 1 wt % ethanol solution with fluoroalkylsilane [FAS, $\text{C}_8\text{F}_{13}\text{H}_4\text{Si}(\text{OCH}_2\text{CH}_3)_3$] for 90 min, to lower the surface energy, and dried at 120°C for 30 min. Homogeneous SLIPS can then be obtained by infusing silicon oil on the as-prepared surface, which was tilted at $\sim 45^\circ$ and held still for 3 h to drain away extra floating oil (Figure S1a).

Fabrication of 3D Topological SLIPS. Sub-millimeter grooved structures were first milled on the polished copper sheets by using a UV laser marking machine (KY-M-UV3L, Wuhan Keyi). The frequency of 40 Hz and the pulse width of $1 \mu\text{s}$ were held constant during the process. The milled sample was then ultrasonically cleaned in DI water to remove impurities and oxide layers before being subjected to the oxidation process, chemical modification, and silicon oil infusion in sequence to obtain the ultraslippery property, as shown in Figure S1b.

Characterization. The micromorphology and 3D profile of the as-prepared surface were analyzed using a scanning electron microscope (SEM, Ultra60, Zeiss), a digital microscope (VHX-600, Keyence), and an optical profiling system (ContourGT-K, Bruker), respectively. The crystal structures and elements of the surface were characterized with X-ray diffraction (XRD-6000) and energy-dispersive spectroscopy (EDS, Ultim Max), respectively. Static and dynamic contact angles were characterized with a goniometer (Rame-Hart 290). Sliding angles were measured with a vertically mounted rotary table. Sliding resistance was obtained by the measured sliding angles and force equilibrium equation. Images and videos of the droplet motion on the SLIPS were taken by a digital camera with 1000 fps high-speed recording function (RX100M5, Sony).

ASSOCIATED CONTENT

Supporting Information

The Supporting Information is available free of charge at <https://pubs.acs.org/doi/10.1021/acsnano.0c07417>.

Schematic of fabricating SLIPS. Optical micrograph of the lubricating layer. SEM images of the laser-treated surface. Experimental optical photos of droplet impacting on SLIPS and a superhydrophobic surface. Optical images of the grooves with different widths and depths. Sliding resistance and droplet motion control of droplets of different solutions. Droplet storage and mixing on the as-prepared grooved nanotextured SLIPS. Sliding resistance on the grooved nanotextured SLIPS that were infused with different liquids (PDF)

Water droplet sliding on a gradually tilted nanotextured SLIPS (MP4)

Water droplet sliding inside SLIPS while pinned at the edge (MP4)

Water droplet transporting on an upside-down SLIPS (MP4)

Efficient and precise droplet transporting on grooved nanotextured SLIPS (MP4)

Spontaneous droplet transporting on wedge-shaped nanotextured SLIPS (MP4)

Flow of oil lubricating film on the cloaked droplet interface (MP4)

Droplet adhering in the grooves of grooved nanotextured SLIPS (MP4)

Droplet sliding off a gradually tilted grooved nanotextured SLIPS with different groove widths (MP4)

Droplet transporting along winding grooved nanotextured SLIPS (MP4)

Dynamic behavior of droplets impacting on the grooved nanotextured SLIPS (MP4)

Transporting droplets of different solutions on the grooved nanotextured SLIPS (MP4)

Droplet mixing and transporting on the grooved nanotextured SLIPS (MP4)

Droplet transporting on strip-ridge-shaped nanotextured SLIPS (MP4)

Droplet transporting on ionic liquid-infused grooved nanotextured SLIPS (MP4)

AUTHOR INFORMATION

Corresponding Authors

Xiaolei Wang – National Key Laboratory of Science and Technology on Helicopter Transmission, Nanjing University of Aeronautics and Astronautics, Nanjing 210016, P. R. China; orcid.org/0000-0002-9055-1011; Email: wxl@nuaa.edu.cn

Yao Lu – Department of Chemistry, School of Biological and Chemical Sciences, Queen Mary University of London, London E1 4NS, U.K.; orcid.org/0000-0001-9566-4122; Email: yao.lu@qmul.ac.uk

Authors

Xiaolong Yang – National Key Laboratory of Science and Technology on Helicopter Transmission, Nanjing University of Aeronautics and Astronautics, Nanjing 210016, P. R. China; orcid.org/0000-0002-2324-6172

Kai Zhuang – National Key Laboratory of Science and Technology on Helicopter Transmission, Nanjing University of Aeronautics and Astronautics, Nanjing 210016, P. R. China

Complete contact information is available at: <https://pubs.acs.org/10.1021/acsnano.0c07417>

Author Contributions

X.Y. proposed the initial idea; X.Y. and Y.L. designed the experiment and analyzed the results; K.Z. fabricated topological SLIPS samples and characterized the droplet dynamic behavior. X.W. supervised the project and provided critical suggestions. X.Y., Y.L., and X.W. drafted the manuscript, and all authors revised the manuscript.

Notes

The authors declare no competing financial interest.

ACKNOWLEDGMENTS

This research was financially supported by the National Natural Science Foundation of China (NSFC, 51905267),

Natural Science Foundation of Jiangsu Province (BK20192007, BK20190411). Y.L. acknowledges the support from the Royal Society Research Grant (RGS\R1\201071).

REFERENCES

- (1) Liu, M. J.; Wang, S. T.; Jiang, L. Nature-Inspired Superwettability Systems. *Nat. Rev. Mater.* **2017**, *2*, 17036.
- (2) Chen, H. W.; Zhang, P. F.; Zhang, L. W.; Liu, H. L.; Jiang, Y.; Zhang, D. Y.; Han, Z. W.; Jiang, L. Continuous Directional Water Transport on the Peristome Surface of *Nepenthes Alata*. *Nature* **2016**, *532*, 85–89.
- (3) Cira, N. J.; Benusiglio, A.; Prakash, M. Vapour-Mediated Sensing and Motility in Two-Component Droplets. *Nature* **2015**, *519*, 446–450.
- (4) Zheng, Y. M.; Bai, H.; Huang, Z. B.; Tian, X. L.; Nie, F. Q.; Zhao, Y.; Zhai, J.; Jiang, L. Directional Water Collection on Wetted Spider Silk. *Nature* **2010**, *463*, 640–643.
- (5) Huang, W.-P.; Chen, X.; Hu, M.; Hu, D.-F.; Wang, J.; Li, H.-Y.; Ren, K.-F.; Ji, J. Patterned Slippery Surface through Dynamically Controlling Surface Structures for Droplet Microarray. *Chem. Mater.* **2019**, *31*, 834–841.
- (6) Xing, D.; Wang, R.; Wu, F.; Gao, X. Confined Growth and Controlled Coalescence/Self-Removal of Condensate Microdrops on a Spatially Heterogeneously Patterned Superhydrophilic-Superhydrophobic Surface. *ACS Appl. Mater. Interfaces* **2020**, *12*, 29946–29952.
- (7) Nasser, J.; Lin, J.; Zhang, L.; Sodano, H. A. Laser Induced Graphene Printing of Spatially Controlled Super-Hydrophobic/Hydrophilic Surfaces. *Carbon* **2020**, *162*, 570–578.
- (8) Nishikawa, N.; Kiyohara, H.; Sakiyama, S.; Yamazoe, S.; Mayama, H.; Tsujioka, T.; Kojima, Y.; Yokojima, S.; Nakamura, S.; Uchida, K. Photoinduced Formation of Superhydrophobic Surface on Which Contact Angle of a Water Droplet Exceeds 170 Degrees by Reversible Topographical Changes on a Diethylene Microcrystalline Surface. *Langmuir* **2012**, *28*, 17817–17824.
- (9) Ichimura, K.; Oh, S. K.; Nakagawa, M. Light-Driven Motion of Liquids on a Photoresponsive Surface. *Science* **2000**, *288*, 1624–1626.
- (10) Dai, H.; Gao, C.; Sun, J.; Li, C.; Li, N.; Wu, L.; Dong, Z.; Jiang, L. Controllable High-Speed Electrostatic Manipulation of Water Droplets on a Superhydrophobic Surface. *Adv. Mater.* **2019**, *31*, 1905449.
- (11) Sun, Q.; Wang, D.; Li, Y.; Zhang, J.; Ye, S.; Cui, J.; Chen, L.; Wang, Z.; Buett, H.-J.; Vollmer, D.; Deng, X. Surface Charge Printing for Programmed Droplet Transport. *Nat. Mater.* **2019**, *18*, 936–941.
- (12) Li, C.; Guo, R.; Jiang, X.; Hu, S.; Li, L.; Cao, X.; Yang, H.; Song, Y.; Ma, Y.; Jiang, L. Reversible Switching of Water-Droplet Mobility on a Superhydrophobic Surface Based on a Phase Transition of a Side-Chain Liquid-Crystal Polymer. *Adv. Mater.* **2009**, *21*, 4254–4258.
- (13) Yang, C.; Wu, L.; Li, G. Magnetically Responsive Superhydrophobic Surface: *In Situ* Reversible Switching of Water Droplet Wettability and Adhesion for Droplet Manipulation. *ACS Appl. Mater. Interfaces* **2018**, *10*, 20150–20158.
- (14) Zahner, D.; Abagat, J.; Svec, F.; Frechet, J. M. J.; Levkin, P. A. A Facile Approach to Superhydrophilic-Superhydrophobic Patterns in Porous Polymer Films. *Adv. Mater.* **2011**, *23*, 3030–3034.
- (15) Li, Y.; He, L.; Zhang, X.; Zhang, N.; Tian, D. External-Field-Induced Gradient Wetting for Controllable Liquid Transport: From Movement on the Surface to Penetration into the Surface. *Adv. Mater.* **2017**, *29*, 1703802.
- (16) Wu, D.; Wu, S. Z.; Chen, Q. D.; Zhang, Y. L.; Yao, J.; Yao, X.; Niu, L. G.; Wang, J. N.; Jiang, L.; Sun, H. B. Curvature-Driven Reversible *In Situ* Switching between Pinned and Roll-Down Superhydrophobic States for Water Droplet Transportation. *Adv. Mater.* **2011**, *23*, 545–549.
- (17) Wong, T.-S.; Kang, S. H.; Tang, S. K. Y.; Smythe, E. J.; Hatton, B. D.; Grinthal, A.; Aizenberg, J. Bioinspired Self-Repairing Slippery Surfaces with Pressure-Stable Omniphobicity. *Nature* **2011**, *477*, 443–447.

- (18) Dai, X.; Stogin, B. B.; Yang, S.; Wong, T.-S. Slippery Wenzel State. *ACS Nano* **2015**, *9*, 9260–9267.
- (19) Zhang, C.; Zhang, B.; Ma, H.; Li, Z.; Xiao, X.; Zhang, Y.; Cui, X.; Yu, C.; Cao, M.; Jiang, L. Bioinspired Pressure-Tolerant Asymmetric Slippery Surface for Continuous Self-Transport of Gas Bubbles in Aqueous Environment. *ACS Nano* **2018**, *12*, 2048–2055.
- (20) Zheng, Y. F.; Cheng, J.; Zhou, C. L.; Xing, H. T.; Wen, X. F.; Pi, P. H.; Xu, S. P. Droplet Motion on a Shape Gradient Surface. *Langmuir* **2017**, *33*, 4172–4177.
- (21) Park, K.-C.; Kim, P.; Grinthal, A.; He, N.; Fox, D.; Weaver, J. C.; Aizenberg, J. Condensation on Slippery Asymmetric Bumps. *Nature* **2016**, *531*, 78–82.
- (22) Ling, S.; Luo, Y.; Luan, L.; Wang, Z.; Wu, T. Inkjet Printing of Patterned Ultra-Slippery Surfaces for Planar Droplet Manipulation. *Sens. Actuators, B* **2016**, *235*, 732–738.
- (23) Luo, H.; Lu, Y.; Yin, S.; Huang, S.; Song, J.; Chen, F.; Chen, F.; Carmalt, C. J.; Parkin, I. P. Robust Platform for Water Harvesting and Directional Transport. *J. Mater. Chem. A* **2018**, *6*, 5635–5643.
- (24) Manabe, K.; Matsubayashi, T.; Tenjimbayashi, M.; Moriya, T.; Tsuge, Y.; Kyung, K.-H.; Shiratori, S. Controllable Broadband Optical Transparency and Wettability Switching of Temperature Activated Solid/Liquid-Infused Nanofibrous Membranes. *ACS Nano* **2016**, *10*, 9387–9396.
- (25) Bjelobrk, N.; Girard, H.-L.; Bengaluru Subramanyam, S.; Kwon, H.-M.; Quere, D.; Varanasi, K. K. Thermocapillary Motion on Lubricant-Impregnated Surfaces. *Phys. Rev. Fluids* **2016**, *1*, 063902.
- (26) Gao, C.; Wang, L.; Lin, Y.; Li, J.; Liu, Y.; Li, X.; Feng, S.; Zheng, Y. Droplets Manipulated on Photothermal Organogel Surfaces. *Adv. Funct. Mater.* **2018**, *28*, 1803072.
- (27) Che, P.; Heng, L.; Jiang, L. Lubricant-Infused Anisotropic Porous Surface Design of Reduced Graphene Oxide toward Electrically Driven Smart Control of Conductive Droplets' Motion. *Adv. Funct. Mater.* **2017**, *27*, 1606199.
- (28) Oh, I.; Keplinger, C.; Cui, J.; Chen, J.; Whitesides, G. M.; Aizenberg, J.; Hu, Y. Dynamically Actuated Liquid-Infused Poroelastic Film with Precise Control over Droplet Dynamics. *Adv. Funct. Mater.* **2018**, *28*, 1802632.
- (29) Brabcova, Z.; McHale, G.; Wells, G. G.; Brown, C. V.; Newton, M. I. Electric Field Induced Reversible Spreading of Droplets into Films on Lubricant Impregnated Surfaces. *Appl. Phys. Lett.* **2017**, *110*, 121603.
- (30) He, X.; Qiang, W.; Du, C.; Shao, Q.; Zhang, X.; Deng, Y. Modification of Lubricant Infused Porous Surface for Low-Voltage Reversible Electrowetting. *J. Mater. Chem. A* **2017**, *5*, 19159–19167.
- (31) Han, K.; Heng, L.; Zhang, Y.; Liu, Y.; Jiang, L. Slippery Surface Based on Photoelectric Responsive Nanoporous Composites with Optimal Wettability Region for Droplets' Multifunctional Manipulation. *Adv. Sci.* **2019**, *6*, 1801231.
- (32) Guo, P.; Wang, Z.; Heng, L.; Zhang, Y.; Wang, X.; Jiang, L. Magnetocontrollable Droplet and Bubble Manipulation on a Stable Amphibious Slippery Gel Surface. *Adv. Funct. Mater.* **2019**, *29*, 1808717.
- (33) Khalil, K. S.; Mahmoudi, S. R.; Abu-dheir, N.; Varanasi, K. K. Active Surfaces: Ferrofluid-Impregnated Surfaces for Active Manipulation of Droplets. *Appl. Phys. Lett.* **2014**, *105*, 041604.
- (34) Rigoni, C.; Ferraro, D.; Carlassara, M.; Filippi, D.; Varagnolo, S.; Pierno, M.; Talbot, D.; Abou-Hassan, A.; Mistura, G. Dynamics of Ferrofluid Drops on Magnetically Patterned Surfaces. *Langmuir* **2018**, *34*, 8917–8922.
- (35) Wang, W.; Timonen, J. V. I.; Carlson, A.; Drotlef, D.-M.; Zhang, C. T.; Kolle, S.; Grinthal, A.; Wong, T.-S.; Hatton, B.; Kang, S. H.; Kennedy, S.; Chi, J.; Blough, R. T.; Sitti, M.; Mahadevan, L.; Aizenberg, J. Multifunctional Ferrofluid-Infused Surfaces with Reconfigurable Multiscale Topography. *Nature* **2018**, *559*, 77–82.
- (36) Wu, D.; Wang, J.-N.; Wu, S.-Z.; Chen, Q.-D.; Zhao, S.; Zhang, H.; Sun, H.-B.; Jiang, L. Three-Level Biomimetic Rice-Leaf Surfaces with Controllable Anisotropic Sliding. *Adv. Funct. Mater.* **2011**, *21*, 2927–2932.
- (37) Xu, T.; Song, Y.; Gao, W.; Wu, T.; Xu, L.-P.; Zhang, X.; Wang, S. Superwetttable Electrochemical Biosensor toward Detection of Cancer Biomarkers. *ACS Sensors* **2018**, *3*, 72–78.
- (38) Seo, J.; Lee, J. S.; Lee, K.; Kim, D.; Yang, K.; Shin, S.; Mahata, C.; Jung, H. B.; Lee, W.; Cho, S.-W.; Lee, T. Switchable Water-Adhesive, Superhydrophobic Palladium-Layered Silicon Nanowires Potentiate the Angiogenic Efficacy of Human Stem Cell Spheroids. *Adv. Mater.* **2014**, *26*, 7043–7050.
- (39) Wen, X. G.; Zhang, W. X.; Yang, S. H. Synthesis of Cu(OH)(2) and CuO Nanoribbon Arrays on a Copper Surface. *Langmuir* **2003**, *19*, 5898–5903.
- (40) Cudennec, Y.; Lecerf, A. The Transformation of Cu(OH)(2) into CuO, Revisited. *Solid State Sci.* **2003**, *5*, 1471–1474.
- (41) Feng, L. L.; Wang, R.; Zhang, Y. Y.; Ji, S. P.; Chuan, Y. M.; Zhang, W.; Liu, B.; Yuan, C.; Du, C. X. *In Situ* XRD Observation of CuO Anode Phase Conversion in Lithium-Ion Batteries. *J. Mater. Sci.* **2019**, *54*, 1520–1528.
- (42) Ma, N.; Cheng, D.; Zhang, J.; Zhao, S.; Lu, Y. A Simple, Inexpensive and Environmental-Friendly Electrochemical Etching Method to Fabricate Superhydrophobic GH4169 Surfaces. *Surf. Coat. Technol.* **2020**, *399*, 126180.
- (43) Kim, P.; Kreder, M. J.; Alvarenga, J.; Aizenberg, J. Hierarchical or Not? Effect of the Length Scale and Hierarchy of the Surface Roughness on Omniphobicity of Lubricant-Infused Substrates. *Nano Lett.* **2013**, *13*, 1793–1799.
- (44) Zhou, L. W.; Xue, H. T.; Fang, Z. N.; Yang, Y.; Huang, J. P. Contact Angle Determined by Spontaneous Dynamic Capillary Rises with Hydrostatic Effects: Experiment and Theory. *Chem. Phys. Lett.* **2006**, *432*, 326–330.
- (45) Smith, J. D.; Dhiman, R.; Anand, S.; Reza-Garduno, E.; Cohen, R. E.; McKinley, G. H.; Varanasi, K. K. Droplet Mobility on Lubricant-Impregnated Surfaces. *Soft Matter* **2013**, *9*, 1772–1780.
- (46) Mumm, F.; van Helvoort, A. T.; Sikorski, P. Easy Route to Superhydrophobic Copper-Based Wire-Guided Droplet Microfluidic Systems. *ACS Nano* **2009**, *3*, 2647–2652.
- (47) Bangham, D.; Razouk, R. Adsorption and the Wettability of Solid Surfaces. *Trans. Faraday Soc.* **1937**, *33*, 1459–1463.
- (48) Lu, Y.; Sathasivam, S.; Song, J.; Crick, C. R.; Carmalt, C. J.; Parkin, I. P. Robust Self-Cleaning Surfaces That Function When Exposed to Either Air or Oil. *Science* **2015**, *347*, 1132–1135.
- (49) Balu, B.; Berry, A. D.; Hess, D. W.; Breedveld, V. Patterning of Superhydrophobic Paper to Control the Mobility of Micro-Liter Drops for Two-Dimensional Lab-on-Paper Applications. *Lab Chip* **2009**, *9*, 3066–3075.
- (50) Yang, X.; Song, J.; Zheng, H.; Deng, X.; Liu, X.; Lu, X.; Sun, J.; Zhao, D. Anisotropic Sliding on Dual-Rail Hydrophilic Tracks. *Lab Chip* **2017**, *17*, 1041–1050.
- (51) Furmidge, C. Studies at Phase Interfaces. I. The Sliding of Liquid Drops on Solid Surfaces and a Theory for Spray Retention. *J. Colloid Sci.* **1962**, *17*, 309–324.
- (52) Yang, X.; Liu, X.; Lu, Y.; Song, J.; Huang, S.; Zhou, S.; Jin, Z.; Xu, W. Controllable Water Adhesion and Anisotropic Sliding on Patterned Superhydrophobic Surface for Droplet Manipulation. *J. Phys. Chem. C* **2016**, *120*, 7233–7240.
- (53) Bier, M.; Dietrich, S. Vapour Pressure of Ionic Liquids. *Mol. Phys.* **2010**, *108*, 211–214.
- (54) Anand, S.; Paxson, A. T.; Dhiman, R.; Smith, J. D.; Varanasi, K. K. Enhanced Condensation on Lubricant-Impregnated Nanotextured Surfaces. *ACS Nano* **2012**, *6*, 10122–10129.